ACS NANO

www.acsnano.org

ARTICLE

Role of Bilayer Graphene Microstructure on the Nucleation of WSe_2 Overlayers

Saiphaneendra Bachu, Malgorzata Kowalik, Benjamin Huet, Nadire Nayir, Swarit Dwivedi, Danielle Reifsnyder Hickey, Chenhao Qian, David W. Snyder, Slava V. Rotkin, Joan M. Redwing, Adri C. T. van Duin, and Nasim Alem*

Cite This: *ACS Nano* 2023, 17, 12140–12150

Read Online

ACCESS | Metrics & More | Article Recommendations | Supporting Information

ABSTRACT: Over the past few years, graphene grown by chemical vapor deposition (CVD) has gained prominence as a template to grow transition metal dichalcogenide (TMD) overlayers. The resulting two-dimensional (2D) TMD/graphene vertical heterostructures are attractive for optoelectronic and energy applications. However, the effects of the microstructural heterogeneities of graphene grown by CVD on the growth of the TMD overlayers are relatively unknown. Here, we present a detailed investigation of how the stacking order and twist angle of CVD graphene influence the nucleation of WSe_2 triangular crystals. Through the combination of experiments and theory, we correlate the presence of interlayer dislocations in bilayer graphene with how WSe_2 nucleates, in agreement with the observation of a higher nucleation density of WSe_2 on top of Bernal-stacked bilayer graphene versus twisted bilayer graphene. Scanning/transmission electron microscopy (S/TEM) data show that interlayer dislocations are present only in Bernal-stacked bilayer graphene but not in twisted bilayer graphene. Atomistic ReaxFF reactive force field molecular dynamics simulations reveal that strain relaxation promotes the formation of these interlayer dislocations with localized buckling in Bernal-stacked bilayer graphene, whereas the strain becomes distributed in twisted bilayer graphene. Furthermore, these localized buckles in graphene are predicted to serve as thermodynamically favorable sites for binding WSe_x molecules, leading to the higher nucleation density of WSe_2 on Bernal-stacked graphene. Overall, this study explores synthesis–structure correlations in the WSe_2/graphene vertical heterostructure system toward the site-selective synthesis of TMDs by controlling the structural attributes of the graphene substrate.

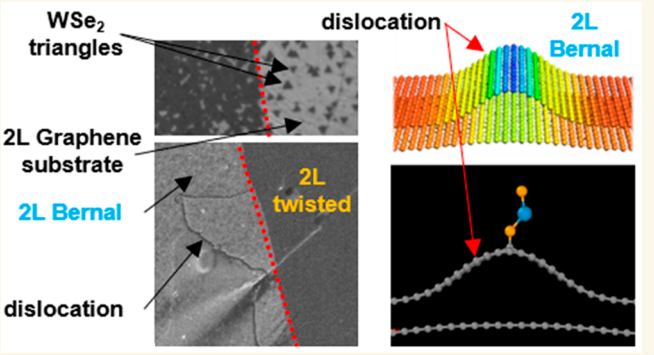

KEYWORDS: *vertical heterostructures, twisted bilayer graphene, Bernal stacking, dark-field transmission electron microscopy, interlayer dislocations, ReaxFF reactive molecular dynamics simulations*

Over the past decade or so, two-dimensional (2D) transition metal dichalcogenides (TMDs) have been discovered[1] and widely studied for various optoelectronic applications.[2−5] They show incredible promise at the proof-of-concept level, owing to their wide-ranging properties such as a tunable band gap,[4] large surface-to-volume ratio,[6] and large exciton binding energies.[7,8] To translate their extraordinary performance to the industrial scale, large-area and uniform synthesis is necessary.[9] Large-area synthesis of TMDs was originally realized by adopting bottom-up techniques such as chemical vapor deposition (CVD) using powder precursors.[10,11] Building on that, improved methods have involved switching to gaseous precursors (e.g., metal−organic chemical vapor deposition, or MOCVD),[12] using symmetry-matched growth substrates (c-plane sapphire and other 2D materials)[13,14] and utilizing growth promoters (salts and PTAS).[15] Among them, MOCVD growth of TMDs on 2D material substrates (e.g., graphene, hBN) is particularly attractive because it offers the combined advantages of precise control of gas precursors and atomically flat surfaces of 2D substrates to enable large-area van der Waals epitaxy.[14,16−18] Moreover, TMD growth on graphene results in the formation of TMD/graphene vertical heterostructures, enabling applications such as multicomponent optoelectronic devices, batteries, and

Received: December 20, 2022
Accepted: June 12, 2023
Published: June 27, 2023

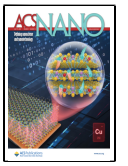

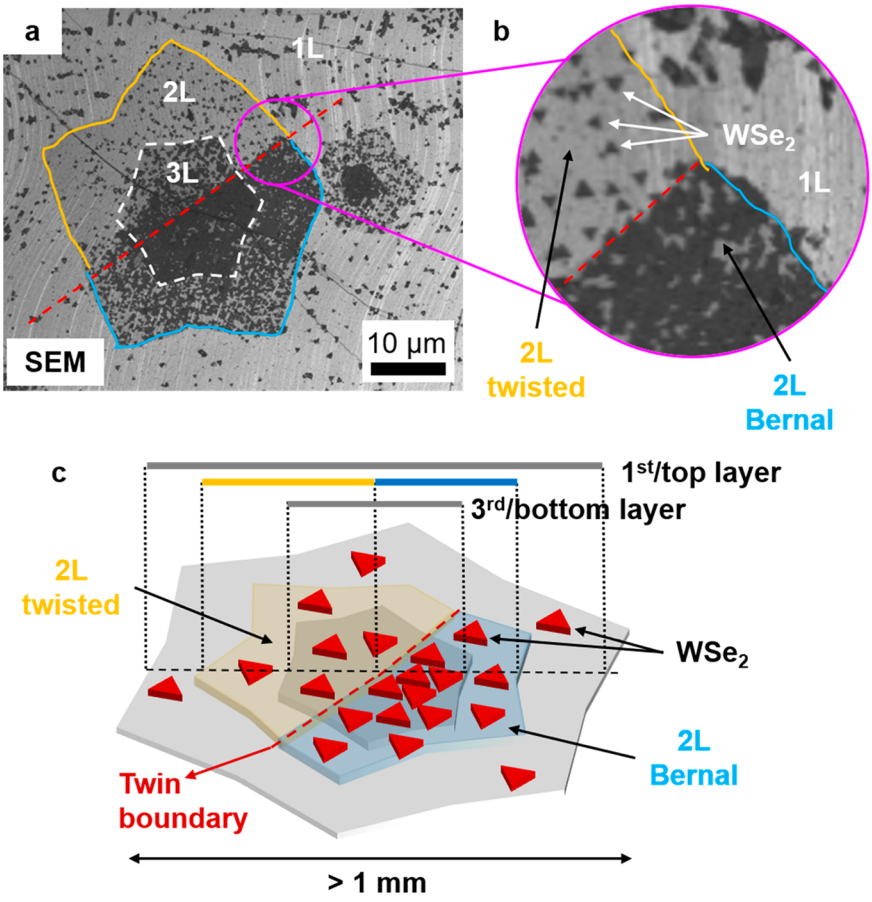

Figure 1. Preferential nucleation of WSe_2 on Bernal-stacked bilayer graphene. (a) Plan-view SEM image of the WSe_2/graphene vertical heterostructure, wherein the trilayer graphene (3L) shows a twin grain boundary (dashed red line) in the second layer of graphene (2L). As a result, the bilayer graphene area to the bottom-right side of the red line (blue outline) contains Bernal stacking, and the top-left side (orange outline) contains twisted bilayer graphene. (b) Enlarged SEM image of the area inside the magenta circle from (a), showing higher WSe_2 triangle density in Bernal-stacked graphene ("2L Bernal") compared to twisted bilayer graphene ("2L twisted"). (c) Schematic illustrating the "inverted wedding cake" structure of 3L graphene and the density variation of WSe_2 (red triangles). The topmost graphene layer (1L) is larger than 1 mm in lateral size.

lasers.[19−22] For example, the WSe_2/graphene heterostructure system is shown to be suitable for p-type field-effect transistor (FET) devices with low contact resistance.[23−25]

Despite the promise of large-area TMD/graphene vertical heterostructures, it has recently been uncovered that the heterogeneities in the graphene substrate can have a pronounced effect on the nucleation and growth behavior of TMD overlayers.[26−28] For example, Azizi et al.[26] observed that grain boundaries in freestanding graphene act as extra nucleation sites and favor the growth of multilayer WSe_2 crystals. Kim et al.[27] discovered that defective areas in the graphene substrate strongly interact with the WS_2 epilayers via covalent bonding and cause the WS_2 to exhibit different intrinsic properties. These examples highlight the need for a fundamental understanding of how the heterogeneities in graphene could affect the TMD overlayer growth. While defect structures and their effects on TMD overlayer growth in single-layer graphene are well studied,[26−29] multilayer graphene is relatively less explored. In this regard, CVD growth of graphene emerged as a promising method to produce highly crystalline multilayer graphene with a wide variety of layer numbers, stacking orders, and twist angles.[30−32] Consequently, these attributes lead to various structural defects, strain states, and local atomic reconstructions in the as-grown multilayer graphene.[33−36] The presence of these heterogeneities could offer additional degrees of freedom in tuning the TMD overlayer growth and, consequently, the properties of as-grown vertical heterostructures.

Interestingly, it was recently discovered that the growth of WSe_2 is strongly affected by the stacking order and twist angle of the CVD graphene substrate.[37] This previous work showed that the WSe_2 triangular crystals grow preferentially with higher nucleation density on top of Bernal-stacked bilayer graphene than on twisted bilayer graphene in a multilayer graphene island. To reveal the origin behind this observation, we present a systematic characterization of a bilayer graphene substrate before and after WSe_2 growth. We then link the characterization results to atomistic simulations to establish synthesis−structure correlations for the as-grown WSe_2/graphene vertical heterostructures. First, scanning/transmission electron microscopy (S/TEM) imaging and selected area electron diffraction (SAED) are employed to confirm the layer number, stacking order, and twist angle of the bilayer graphene. Next, dark-field transmission electron microscopy (DFTEM) is used to reveal the microstructural differences between Bernal-stacked and twisted bilayer graphene. Subsequently, ReaxFF reactive force field molecular dynamics simulations[38] are used to model the atomic structure of the

https://doi.org/10.1021/acsnano.2c12621
ACS Nano 2023, 17, 12140−12150

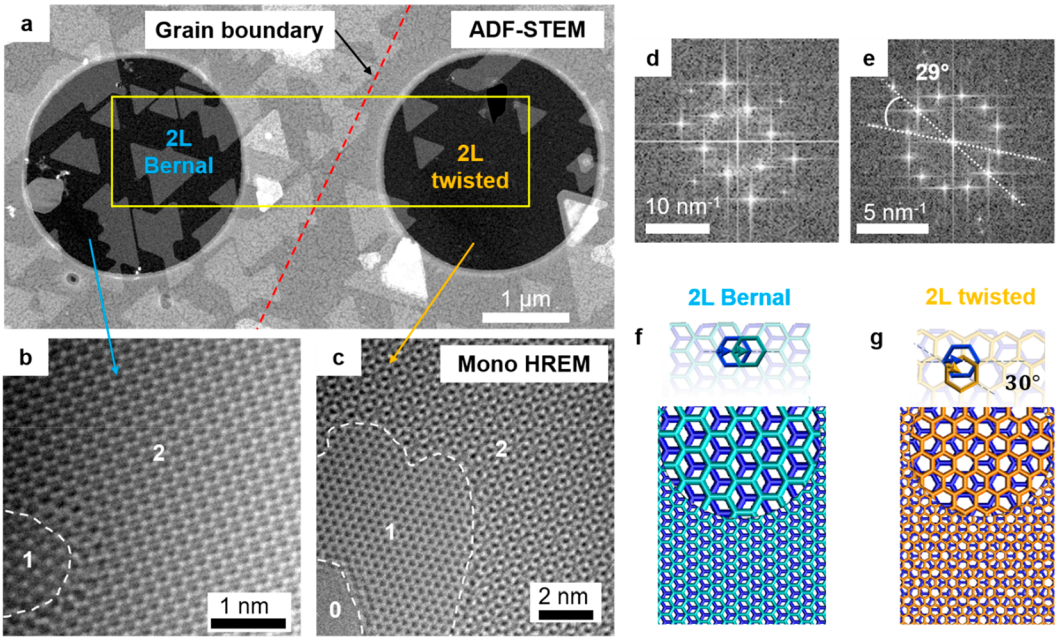

Figure 2. Confirmation of layer number and stacking across a twin grain boundary in 2L graphene. (a) ADF-STEM image of the WSe_2/graphene vertical heterostructure showing the density variation of WSe_2 across a twin grain boundary in the 2L graphene area, which is similar to the one seen in Figure 1. (b, c) Monochromated HREM images of "2L Bernal" (b) and "2L twisted" (c) regions showing two graphene layers and confirming the corresponding stacking order. (d, e) The FFT patterns obtained from "2L Bernal" (d) and "2L twisted" (e) regions, confirming the oriented and twisted nature of corresponding regions. The twist angle measured from (e) is 29°. (f, g) The atomistic models representing Bernal-stacked (f) and 30° twisted bilayer graphene (g).

experimentally observed graphene bilayers. Finally, these ReaxFF simulations are used to calculate the binding energies of WSe_x clusters to these graphene structures to propose possible atomistic mechanisms responsible for the preferential growth of WSe_2 on Bernal-stacked bilayer graphene.

RESULTS AND DISCUSSION

The WSe_2/graphene vertical heterostructures studied here are synthesized using a two-step gas-source CVD process. Their detailed synthesis protocol along with the scanning electron microscopy (SEM), atomic force microscopy (AFM), Raman spectroscopy, and photoluminescence (PL) characterization can be found elsewhere[37] (also, see Methods section). Figure 1a shows a plan-view SEM image of a trilayer graphene island where the second (2L) and third (3L) graphene layers form underneath the first grown graphene layer (1L) during the CVD process, thus forming the so-called "inverted wedding cake" structure.[30,39−42] As seen from Figure 1a, there is a grain boundary going through the second layer of graphene, indicated by a dashed red line. This is evident from two observations. First, the edges of the second and third layers are parallel to each other on the bottom right side of the dashed red line but not on the top-left side of the red line, and (ii) the shape of the third layer is symmetrical, whereas the second layer has an asymmetrical shape. We can also infer from these observations that the bottom-right half of the 2L region (blue outline) has Bernal-stacked bilayer graphene where the two layers are oriented with each other (referred to as "2L Bernal" from here on). In contrast, the top-left half of the 2L region (orange outline) has misoriented/twisted bilayer graphene (referred to as "2L twisted" from here on). Such a grain boundary is called a twin grain boundary and is typically formed when a single nucleation site gives rise to a domain with two different orientations. This type of grain boundary is unlike typical grain boundaries that form upon coalescence of two adjacent graphene domains. Figure 1b magnifies a small region outlined with a magenta circle in Figure 1a, which contains "2L Bernal", "2L twisted", and the 1L−2L graphene layer step edge. It is apparent from this figure that the WSe_2 crystals grown on top of graphene (dark triangles of ∼500 nm in size) exhibit two preferred epitaxial orientations rotated by a 60°, which is commonly observed during MOCVD growth of TMDs on symmetry-matched substrates.[26,43] A closer look at the image reveals that the WSe_2 triangle density on top of "2L Bernal" is significantly higher compared to that on "2L twisted". It should be noted that this observation is universal in our synthesis and applies to separately grown Bernal-stacked and twisted bilayer islands, as well.[37] However, this particular island is chosen here, because it readily conveys the observation. Also, the proximity of two types of bilayer structures makes it easier to find such an island inside TEM (explained in detail in the Methods section). This observation is also illustrated by using a schematic of the as-grown vertical heterostructure in Figure 1c. The following sections focus on comprehensive characterization of the graphene substrate toward elucidating the fundamental mechanisms responsible for this observation.

Before exploring the origin behind the WSe_2 nucleation density variation, we first confirmed the layer number and stacking of bilayer graphene across the twin grain boundary using S/TEM imaging. The as-grown WSe_2/graphene vertical heterostructures are transferred to a Quantifoil copper TEM grid using a NaOH-based transfer method (see Methods section). The TEM grid is first scanned using a combination of SAED and low-magnification annular dark-field scanning transmission electron microscopy (ADF-STEM) imaging to find a bilayer graphene area with a twin grain boundary similar

https://doi.org/10.1021/acsnano.2c12621
ACS Nano 2023, 17, 12140−12150

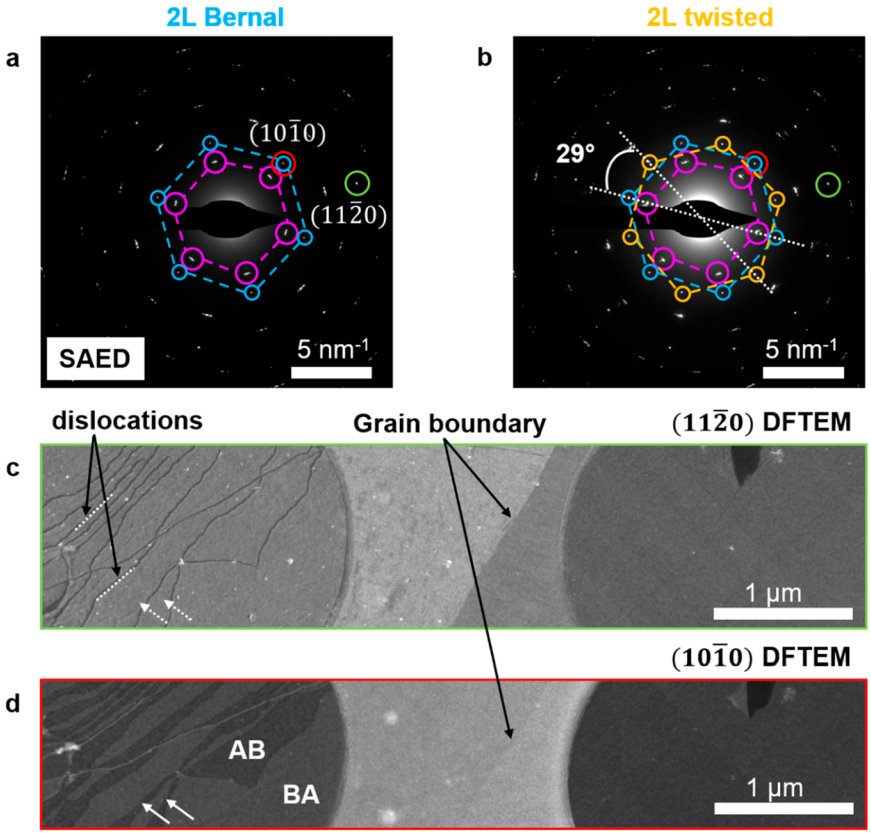

Figure 3. Microstructural differences between Bernal-stacked and twisted bilayer graphene. (a, b) SAED patterns of "2L Bernal" (a) and "2L twisted" (b) regions, confirming the stacking order and twist angle observed with use of the HREM imaging. The SAED patterns also reveal that the WSe2 triangles (dashed magenta hexagon joining six magenta circles) are epitaxial with only the topmost graphene layer (dashed blue hexagon joining the six blue circles). (c, d) DFTEM images obtained from the area inside the yellow rectangle in Figure 2a by using (11$\bar{2}$0) (c) and (10$\bar{1}$0) (d) reflections of the topmost graphene layer. Those reflections are marked by green and red circles in the SAED patterns, respectively. Both the DFTEM images show contrast features in the "2L Bernal" area (interlayer dislocations in the (11$\bar{2}$0) image and AB/BA stacking changes in the (10$\bar{1}$0) image) but not in the "2L twisted" area.

to the one seen in Figure 1 (see Methods section for more details about the scanning procedure). Figure 2a is an ADF-STEM image of the heterostructure showing a twin grain boundary (dashed red line) in a bilayer graphene region. Here, the grain boundary represented by the dashed red line separates the high WSe_2 triangle density region on the left side ("2L Bernal") from the low WSe_2 triangle density region on the right side ("2L twisted"). To confirm the graphene layer number and the stacking in these regions, we used monochromated high-resolution electron microscopy (HREM) imaging. During the collection of HREM images, the sample is exposed to the electron beam for a prolonged time to intentionally create a hole in the film and estimate the number of graphene layers. Here, the holes created on either side of the grain boundary via knock-on sputtering confirm the bilayer nature of the graphene (dashed white outlines in Figure 2b and Figure 2c). Furthermore, the HREM image obtained from the left side of the grain boundary (Figure 2b) shows Bernal stacking of bilayer graphene wherein the carbon atoms of one graphene layer are translated with respect to the other layer by $\frac{1}{3}\langle 10\bar{1}0\rangle$ without any rotational misorientation.[44] The fast Fourier transform (FFT) pattern obtained from this image (Figure 2d) shows only one set of reflections, further confirming that the two graphene layers are oriented with each other. The HREM image obtained from the right side of the grain boundary (Figure 2c) shows a rotational moiré pattern, thus confirming the twisted nature of the bilayer graphene. The FFT pattern of this image (Figure 2e) shows two sets of graphene reflections with a twist angle of 29°. Atomistic models representing the Bernal-stacked and twisted bilayer graphene (30° twist angle) are visualized in Figure 2f and 2g, respectively. More details regarding the considered atomistic models can be found in the Methods section. It is noteworthy that the region shown in Figure 2a is near a trijunction where the grain boundary in the bilayer graphene meets a 1L–2L graphene layer step edge. An ADF-STEM image with a larger field of view showing the trijunction and the HREM characterization from the 1L area is presented in Figure S1.

To determine the orientation relationship between the WSe_2 triangles and the underlying graphene layers in the bilayer region (2L), SAED patterns are acquired. The SAED pattern collected from the "2L Bernal" area of Figure 2a is shown in Figure 3a, whereas the pattern collected from the "2L twisted" area is shown in Figure 3b. These SAED patterns appear similar to their corresponding FFT patterns, as they also display one set (dashed blue hexagon joining the six blue circles) and two sets of graphene reflections (dashed blue and orange hexagons joining the circles of the same color), respectively. Also, the twist angle measured from the SAED pattern of the "2L twisted" area is 29°, proving the angle

https://doi.org/10.1021/acsnano.2c12621
ACS Nano 2023, 17, 12140–12150

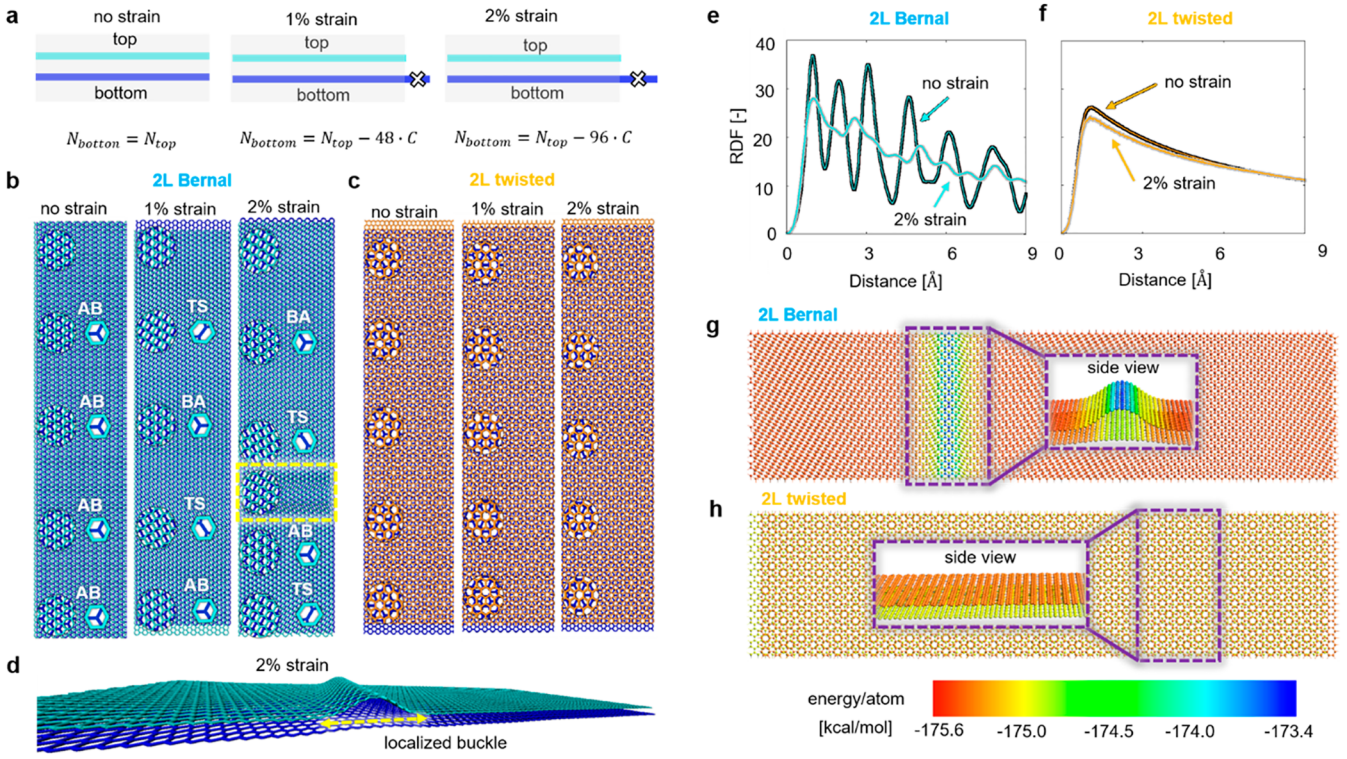

Figure 4. Atomic structural characteristics of Bernal-stacked vs twisted bilayer graphene. (a) Schematic representation of the procedure used to construct models with built-in strain difference between the top and bottom layer, where N_x indicates the total number of atoms in layer x and C indicates a carbon atom. (b, c) Top views of the equilibrated structures for all considered models for Bernal-stacked (b) and twisted (c) bilayers. A perspective view of the "2L Bernal" model with 2% built-in strain difference is given in (d). The RDF curves for atom pairs forming the top and bottom graphene layers for the model with no strain difference are compared to the RDFs for the models with 2% built-in strain difference between the top and bottom layer and presented in (e) for "2L Bernal" and (f) "2L twisted" models. (g, h) Heat maps representing the energy/atom distributions for models with a 2% strain difference for "2L Bernal" (g) and "2L twisted" (h) models. The side views of the parts of the ribbons that form the purple rectangles are shown as the insets; the color scale is given at the bottom.

measured from the corresponding FFT pattern is not an artifact of electron beam knock-on sputtering. Since the topmost graphene layer is single crystalline and spans a lateral size exceeding 1 mm, its reflections are present in both diffraction patterns (dashed blue hexagon). Moreover, in both areas, the WSe_2 reflections (dashed magenta hexagon joining six magenta circles) are epitaxial only with the topmost graphene layer. This indicates that the WSe_2 triangles maintain the orientation relationship with the graphene layer that the transition metal and chalcogen precursors come in direct contact with during the synthesis procedure.[37]

To uncover the possible role of microstructural heterogeneities in graphene behind the WSe_2 triangle density variation, DFTEM imaging is utilized. DFTEM images are acquired from the area inside the yellow rectangle in Figure 2a by placing an objective aperture over the $(11\bar{2}0)$ and $(10\bar{1}0)$ reflections of the topmost graphene layer, i.e., the layer that is epitaxial with WSe_2. These reflections are marked by green and red circles in the SAED patterns in Figure 3a and 3b. The $(11\bar{2}0)$ and $(10\bar{1}0)$ DFTEM images in Figure 3c and 3d are composite images created from three individual DFTEM images which are aligned, stitched together, and cropped to match the area inside the yellow rectangle in Figure 2a (Figure S2 shows the individual DFTEM images used for stitching). The $(11\bar{2}0)$ DFTEM images typically display a sharp contrast when there is a layer number change.[45] In Figure 3c, while the total number of layers is two on either side of the grain boundary, the number of graphene layers that are aligned with WSe_2 (spot chosen for DFTEM) changes from two on the left side to one on the right side. Therefore, this decrease in the layer number causes a decrease in the DFTEM image intensity. Also, the "2L Bernal" region of graphene exhibits strong line-shaped contrast in the top graphene layer. These features have been previously reported in the literature and are referred to as interlayer dislocations, strain solitons, or domain walls.[45−48] These interlayer dislocations are also often associated with strain relaxation in the basal plane of the top graphene layer in the form of out-of-plane displacement of carbon atoms in a localized area and thus are also named "ripplocations".[49−51] In various previous reports, these interlayer dislocations formed by a built-in strain difference between the two layers of bilayer graphene have also been theoretically investigated.[52−57] It must be noted that these dislocations are different from folds and wrinkles[58−60] commonly observed in 2D materials because, unlike them, the interlayer dislocations are associated with periodic stacking changes and have Burgers vectors along particular crystallographic directions.[45] Similarly, these dislocations are different from dislocations seen in single-layer graphene.[61−63] Strikingly, the interlayer dislocations seen in Figure 3c do not propagate through the grain boundary and are absent in the twisted bilayer. This observation suggests a possible difference in the strain relaxation mechanism between Bernal-stacked and twisted bilayer graphene. To verify if the higher WSe_2 nucleation density on Bernal-stacked bilayer

https://doi.org/10.1021/acsnano.2c12621
ACS Nano 2023, 17, 12140−12150

graphene can be correlated with the presence of these interlayer dislocations, ReaxFF reactive force field molecular dynamics simulations are performed (discussed in detail later and presented in Figures 4 and 5).

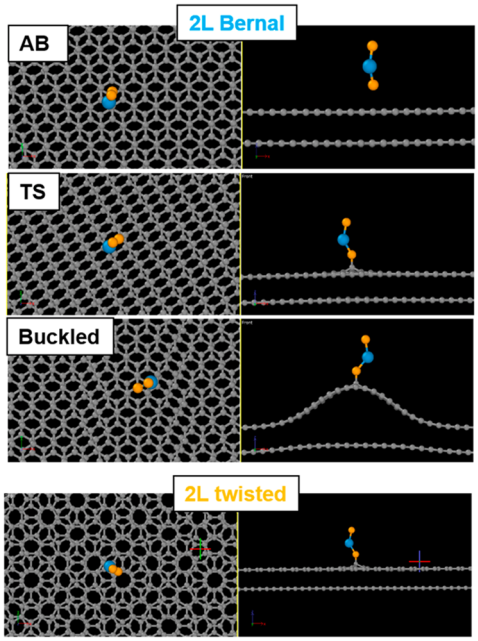

Figure 5. Binding energies of WSe_2 to Bernal-stacked vs twisted bilayer graphene. The top views of the considered minimized structures of WSe_2 at the bilayer surface are shown in the left panel, whereas the side views are shown in the right panel. The carbon atoms are represented as gray, W atoms as blue, and Se atoms as orange spheres in all the panels. Binding energies of WSe_2 to the T1 (one-fold coordinated top) site of the AB stacked region, stacking transition (TS) region between AB and BA stacked regions, buckled region of "2L Bernal" graphene, and twisted bilayer graphene are −1.85, −1.85, −2.50, and −1.76 eV, respectively, showing a similar trend to those of W and WSe_3 in Figure S12 and Table S1.

The $(10\bar{0}0)$ DFTEM image (Figure 3d) also displays a contrast gradient across the grain boundary. The contrast from the "2L Bernal" region in this image appears as dark-to-bright intensity fluctuations rather than dislocation lines, and they again disappear in the "2L twisted" region. These contrast fluctuations correspond to local AB-to-BA Bernal stacking changes with the stacking transitions occurring at the interlayer dislocations.[45−48] Also, the $(10\bar{1}0)$ DFTEM image does not show strong contrast from the layer number change at the grain boundary. This difference in contrast between the two DFTEM images is expected because the $\{10\bar{1}0\}$ reflections of 2D materials are known to be sensitive to stacking changes but not layer number change, and vice versa for $\{11\bar{2}0\}$ reflections.[45,64−66] Another interesting observation here is that not all of the AB-to-BA stacking changes in the $(10\bar{1}0)$ DFTEM image (e.g., solid white arrows in Figure 3d) guarantee the presence of an interlayer dislocation in the $(11\bar{2}0)$ DFTEM image (dotted white arrows in Figure 3c). This is related to the invisibility criteria of dislocations in DFTEM imaging. Dislocations whose Burgers vectors $(\vec{b})$ satisfy the $\vec{g}\cdot\vec{b} = 0$ criterion do not appear in the DFTEM image formed by the $(h\ k\ l)$ reflection with reciprocal vector $\vec{g}$.[45,67] Systematic DFTEM imaging from different $\{11\bar{2}0\}$ reflections reveals that the dislocations are 60° partials with Burgers vectors along $\langle 1\bar{1}00\rangle$, similar to previous reports (Figure S3).[45,54] This observation further proves that the contrast features seen in the DFTEM images here are associated with dislocations with particular Burgers vector directions and not wrinkles and folds in random directions. Individual DFTEM images acquired from this area by placing an objective aperture over the $(11\bar{2}0)$ and $(10\bar{1}0)$ reflections of the second graphene layer, i.e., the layer that is not epitaxial with WSe_2, are presented in Figure S4. DFTEM imaging performed near a "2L Bernal"−3L step edge where the third layer is twisted with respect to the first two layers is shown in Figure S5. The results in Figure S5 are in accordance with the observations from Figure 3, which further highlights that the correlation between the interlayer dislocations and higher WSe_2 nucleation density is not limited to bilayer graphene, and it can be extended to multilayer areas as well. Additional proof for the existence of the dislocations/domain walls is provided by performing scattering-type scanning near-field optical microscopy (sSNOM) on tri- and multilayer graphene islands transferred to a Si substrate before the WSe_2 deposition (Figures S6 and S7).

The built-in strain difference between the graphene layers that causes these dislocations can have multiple origins or contributions. First, it could be induced by the coefficient of thermal expansion (CTE) mismatch between graphene and the copper substrate used for graphene synthesis.[36,45,59,68] It could also be introduced during the transfer of graphene onto the sapphire substrate employed for the MOCVD process. Finally, it could be caused by the CTE between graphene and sapphire during the MOCVD heating/cooling ramps. To determine whether the dislocations are intrinsic to bilayer CVD graphene or caused during the WSe_2 synthesis process, we imaged Bernal-stacked bilayer graphene directly transferred onto a TEM grid after its synthesis on Cu (Figure S8). Figure S8 shows that dislocations are present in Bernal-stacked bilayer graphene prior to WSe_2 growth. We, however, cannot rule out the possibility of additional dislocation formation or dislocation glide during the MOCVD process. To provide an atomistic insight into the possible difference in the strain relaxation between Bernal-stacked and twisted bilayer graphene, we performed ReaxFF reactive force field molecular dynamic simulations. We further correlated these differences with the observed variation in the WSe_2 nucleation density by using binding energy calculations. The ReaxFF parameter set applied for all the simulations is tuned to correctly describe the effect of stacking order and twist angle in various bilayer graphene models, as well as W and Se atom interactions with these models. The details of the force field development can be found in the Supporting Information (SI).

As presented in Figure 2f and 2g, the bilayer graphene models used for the ReaxFF reactive force field molecular dynamic simulations are constructed by stacking two graphene ribbons (see Methods section for a detailed description). Thereafter, to construct models of "2L Bernal" and "2L twisted" bilayers with a built-in strain difference, the bottom layer is subjected to 1% and 2% uniaxial strain along the zigzag direction, and the atoms with coordinates outside the periodic box are removed (Figure 4a). The three panels in Figure 4a present side-view schematics of the three strain configurations considered for the bilayer graphene models. The left panel with zero built-in strain is labeled as "no strain", the center panel with 1% built-in strain is labeled as "1% strain", and the right

https://doi.org/10.1021/acsnano.2c12621
ACS Nano 2023, 17, 12140−12150

panel with 2% built-in strain is labeled as "2% strain". The resulting difference in the number of atoms between the top and bottom graphene layers is indicated below the corresponding panels in the form of equations, with 48 C atoms for "1% strain" and 96 C atoms for "2% strain". The final structures for all six equilibrated models are presented in Figure 4b and 4c. As shown in Figure 4b, only one type of stacking (AB) is observed for the Bernal-stacked "no strain" model. For the two strained "2L Bernal" models, however, we see a clear alternating AB to BA stacking variation, with the stacking transition ("TS") areas in between. These TS regions correspond to the AB/BA stacking boundaries seen in the DFTEM imaging. The atomic structure of a typical TS region, as seen in monochromated HREM imaging, is depicted in Figure S9. Moreover, in the case of the Bernal-stacked "2% strain" model, a localized buckle (dashed yellow rectangle) is also observed for the considered length of the bilayer graphene. An enlarged three-dimensional (3D) view of this model showing the localized buckle of the top layer is presented in Figure 4d. This localized buckle near the TS region is directly associated with a typical interlayer dislocation seen in the DFTEM imaging and helps release the strain energy.[45,48] It should be noted that our ReaxFF simulations involve smaller atomic models (<8000 atoms) and a simple uniaxial strain scheme to identify the effects of strain difference between two graphene layers. Our aim is not to simulate a realistic strain state of as-grown graphene, which could provide more accurate information on the dislocation characteristics such as widths, line directions, or spacings, but would require significantly larger models (e.g., >20,000,000 atoms to model an area of 500 × 500 nm). On the other hand, for all three "2L twisted" models (Figure 4c), we only see spatial stacking changes in the form of a moiré pattern, which is characteristic of the 30° twisted bilayer graphene, without any buckling.

To quantify the structural differences between "2L Bernal" and "2L twisted" bilayers, we compared the radial pair distribution functions (RDF) of the "no strain" and "2% strain" configurations (Figure 4e and 4f). The considered pair of atoms comprises one carbon atom each from the top and bottom graphene layers. The presence of the peaks in Figure 4e indicates clear crystallographic order or interlayer coupling in the "2L Bernal" models, including the strained configuration. In contrast, no such well-defined peaks are observed for the "2L twisted" models (RDF curves for the "1% strain" configurations of both models are presented in Figure S10). The presented data suggest that the interlayer coupling in Bernal-stacked bilayer graphene is still preserved in the presence of strain. In contrast, the two layers are decoupled for the twisted bilayer graphene with or without a built-in strain difference. This interlayer coupling between the graphene layers in Bernal-stacked bilayer graphene could explain the formation of a localized buckle to relax the built-in strain difference and preserve the structural order. To identify the local stress distribution for the equilibrated models, we compared the energy per atom distributions for the "2L Bernal" and "2L twisted" models with a 2% built-in strain difference (Figure 4g and 4h, respectively). These local stress distributions show that in the case of strained "2L Bernal", any excess stress is concentrated in the localized buckle, whereas the surrounding areas remain stress-free. On the other hand, for the strained "2L twisted", the stress is uniformly distributed among all the atoms in each layer. These observations could explain why the interlayer dislocations with localized buckles are only present in Bernal-stacked bilayer graphene but not in the twisted bilayer graphene. The heat maps of energy per atom for all six of the considered models are given in Figure S11.

Lastly, we compared the binding energies of WSe_x (x = 0, 2, 3) molecules to various sites in the flat and buckled parts of the Bernal-stacked and twisted bilayer graphene to identify the thermodynamically most stable site for a WSe_x molecule to chemically adsorb onto the surface (Figures 5 and S12 and Table S1). The WSe_x adsorption onto the locally buckled region of "2L Bernal" is the most thermodynamically stable, followed by the AB/BA and TS regions. The "2L twisted" model is found to be thermodynamically the least favorable for WSe_x nucleation (Figure 5 and S12). This result suggests three points. First, the localized buckles serve as gates to release strain from the layers by increasing the local interlayer distance, which reduces the van der Waals forces keeping the stack together and increases the chemical reactivity toward gas-phase precursors. Second, a greater probability of adatoms deposited on the locally buckled regions of the Bernal-stacked bilayer than on the other competing sites, likely resulting in a denser population of WSe_2 nucleates. Finally, the twisted bilayer graphene experiences residual strain because of the absence of buckling, which reduces the chemical reactivity toward precursors.

CONCLUSIONS

In summary, combined SEM and S/TEM characterization shows that the nucleation density of WSe_2 triangles strongly varies on top of different regions of CVD graphene, which can be correlated with variation in the stacking order and twist angle of the graphene. In particular, we observe preferential growth of WSe_2 on the Bernal-stacked bilayer graphene compared to ∼30° twisted bilayer graphene. DFTEM images reveal the presence of interlayer dislocations, specifically in the Bernal-stacked bilayer graphene but not in the twisted bilayer graphene. The ReaxFF simulations further confirm that a built-in strain difference between the layers can lead to the formation of localized buckles with AB-to-BA stacking transitions, akin to interlayer dislocations, in Bernal-stacked bilayer graphene. Further, the absence of localized buckling in the 30° twisted bilayer graphene is attributed to the lack of interlayer coupling or structural order. The simulations also show the preferential binding of WSe_x molecules to the buckled areas, suggesting a higher nucleation probability on top of Bernal-stacked bilayer graphene compared to twisted bilayer graphene. These observations can be translated to three or more layer areas of CVD graphene as well. Therefore, this study underscores the important role of microstructural heterogeneities of multilayer graphenes in controlling the growth of TMD overlayers for optoelectronic applications. Furthermore, this study shows the potential for site-selective growth of TMDs on multilayer graphene, and most likely other 2D substrates, by controlling the TMD nucleation density via substrate stacking order and twist angle.

METHODS

Synthesis of WSe_2/Graphene Vertical Heterostructures and SEM Characterization. In the first step of WSe_2/graphene vertical heterostructure synthesis, highly crystalline single- to multilayer graphene is produced by CVD on Cu foils using methane as the carbon source.[30] Here, the CVD process has been tailored to achieve millimeter-sized graphene domains. During the CVD process,

https://doi.org/10.1021/acsnano.2c12621
ACS Nano 2023, 17, 12140−12150

monolayer single crystals of graphene are first grown on the Cu surface. After prolonged growth duration, additional smaller domains of graphene form underneath the first layer, resulting in the "inverted wedding cake" structure. Prior to the second step of heterostructure synthesis, multilayer graphene is transferred onto a 2 in. c-plane sapphire wafer using the wet PMMA-assisted method.[69] The graphene-decorated sapphire wafer is then placed in a cold-wall MOCVD system to grow WSe_2 triangles, resulting in the formation of WSe_2/graphene vertical heterostructures. SEM characterization of the as-grown heterostructures is performed using a Zeiss Gemini field-emission scanning electron microscope (FESEM) at an accelerating voltage of 3 kV and ≤4 mm working distance.

TEM Characterization. The as-grown WSe_2/graphene vertical heterostructures are transferred from the sapphire substrate to a TEM grid using a method similar to the one used to transfer the graphene from the copper to the sapphire surface. The only difference here is that a hot NaOH (90 °C) solution is used to separate the heterostructure film from the sapphire instead of the $FeCl_3$ solution that was used to dissolve the copper substrate. Owing to the large (hundreds of μm to a millimeter) sizes and minimal TEM contrast of graphene islands, it is challenging to locate bilayers, especially those with a grain boundary, on the TEM grid. First, we scanned the sample in diffraction mode in the TEM mode to identify twisted bi- and multilayer graphene areas by looking for multiple sets of graphene reflections. Then, ADF-STEM imaging in the surrounding regions is used to find a grain boundary with help from spatial variation in the WSe_2 triangle density (owing to the *Z*-contrast from the heavy atoms of W and Se). Finally, monochromated HREM imaging in those areas is used to confirm the layer number, stacking order, and twist angle of graphene. SAED patterns and DFTEM and ADF-STEM images are collected using a Thermo Fisher TalosX S/TEM microscope operated at an accelerating voltage of 80 kV. DFTEM images are acquired by placing an objective aperture around the desired diffraction spot and using a 10−20 s integration time. Monochromated HREM imaging is performed on a Thermo Fisher Titan^3 G2 S/TEM microscope operated at an accelerating voltage of 80 kV. During the imaging, a monochromator excitation value of 1 is used. The image corrector is tuned such that the spherical aberration (C3) value is set in the range of −10 to −15 μm and the defocus value is adjusted to provide white atom contrast from the carbon atoms in graphene.[70]

sSNOM Characterization. sSNOM was performed with a customized Neaspec microscope using a mid-IR CW laser source by Daylight Solutions (images in Figures S6 and S7 were obtained at 1564 cm^{-1}/6.289 μm). We used ARROW-NCPt probes by Nanoworld (<25 nm nominal radius) with a typical tapping amplitude of ∼100 nm. In pseudo-heterodyne mode (psHet by Neaspec), we measure both amplitude and phase of harmonics of the scattered laser beam modulated with the tapping frequency, related to the complex-valued local optical impedance of the sample. In multilayer graphene, each stacking configuration of graphene layers—as determined by the number of layers and the relative registry between the layers—corresponds to a specific value of optical impedance. Thus, the values of the amplitude and phase (or real and imaginary parts) of the sSNOM signal can be used to quantify the number of layers and distinguish the layer registry.

ReaxFF Simulations. The ReaxFF reactive force field is a bond-order-based method, where a bond order−bond distance relation in correlation with the bond order−bond energy relation allows for the formation and dissociation of bonds during the molecular dynamics simulations. A more in-depth description of the ReaxFF method and a review of its application can be found elsewhere.[38,71,72] The "2L Bernal" and "2L twisted" models of bilayer graphene are constructed by using periodic graphene ribbons with an initial length of 20 nm and width of 5 nm. The "2L Bernal" bilayer graphene is obtained by stacking two layers with the armchair direction as the shorter edges. For the "2L twisted" model, the shorter edge is armchair for the bottom layer and zigzag for the top layer. This alignment results in the bilayer graphene model with a 30° twist angle that is very close to the experimental observation (29° twist angle) and still follows the periodic boundary condition used for the simulations. To generate the strain difference between the two layers, we applied 1% or 2% uniaxial strain to the bottom layer along the longer edge, i.e., the zigzag direction, and removed the atoms from the bottom layer that do not fit into the periodic box with the initial top layer. It is noteworthy that the ReaxFF simulations tend to underestimate the cohesive energy of Bernal-stacked bilayer graphene compared to density function theory (DFT) calculations (−24.9 meV/atom vs −40 meV/atom).[73] Hence the strain values chosen here are higher so as to realize appreciable changes in the atomic structure of the 20 nm long bilayer graphene models. With this approach, we constructed a total of six configurations of the periodic bilayer graphene models with no strain and with a built-in 1% or 2% strain difference between the top and bottom layer. The systems without strain are initially relaxed by optimizing the geometry using the conjugate gradient method and then equilibrated with the use of the NPT ensemble at room temperature (300 K) and 0.1 MPa pressure. All systems with built-in strain are also initially relaxed and equilibrated with use of the NPT ensemble but with the box length set to be the same as for the system without built-in strain to mimic the effect of the copper surface confining the bottom layer during the CVD synthesis. Thereafter, all structures are cooled to 1.0 K with a cooling rate of 1 K/ps to identify the minimum energy state. Lastly, all of these final optimized configurations are used for binding energy calculations. The time step used for all simulations is 0.25 fs, and the damping parameter for the Berendsen thermostat and barostat is 100 fs. The radial distribution functions are calculated for the systems at 300 K using the NVT ensemble for 100 ps. All simulations are performed using the ADF simulation software, and the simulation snapshots are generated using VMD (Visual Molecular Dynamics) or OVITO.[74,75] The heat maps representing the distribution of energy per atom in Figure 4 and Figure S11 are generated using the option available in the ADF software, and more details for these calculations can be found elsewhere.[76−78]

Binding Energy Calculations. Binding energies ($E_{binding}$) of WSe_x (x = 0, 2, 3) molecules to the various sites in the flat and buckled structures for both "2L Bernal" and "2L twisted" bilayers are computed using eq 1 to identify the most thermodynamically stable site to adsorb on the surface (Figures 5 and S12 and Table S1). A 6-fold coordinated hexagonal site (H6) and a 1-fold coordinated top site (T1) are adopted as adsorption sites for W and WSe_x (x = 2, 3), respectively, on graphene.

$$E_{binding} = E_{total} - (E_{graphene} - E_{WSex}) \quad (1)$$

where E_{total}, $E_{graphene}$, and E_{WSex} are the total energies of a system of interest, graphene, and a WSe_x molecule in a vacuum, respectively. These values are obtained from the relaxation calculations at the ReaxFF level by using the molecular dynamics method.

ASSOCIATED CONTENT

Supporting Information

The Supporting Information is available free of charge at https://pubs.acs.org/doi/10.1021/acsnano.2c12621.

Additional S/TEM and sSNOM characterization of graphene before and after WSe_2 growth, binding energies calculated for W and WSe_3 molecules, and details of ReaxFF force field development (PDF)

AUTHOR INFORMATION

Corresponding Author

Nasim Alem − *Department of Materials Science and Engineering, The Pennsylvania State University, University Park, Pennsylvania 16802, United States; 2D Crystal Consortium (2DCC), Materials Research Institute (MRI), The Pennsylvania State University, University Park, Pennsylvania 16802, United States;* orcid.org/0000-0003-0009-349X; Email: nua10@psu.edu

https://doi.org/10.1021/acsnano.2c12621
ACS Nano 2023, 17, 12140−12150

Authors

Saiphaneendra Bachu − *Department of Materials Science and Engineering, The Pennsylvania State University, University Park, Pennsylvania 16802, United States;* orcid.org/0000-0001-9898-7349

Malgorzata Kowalik − *Department of Mechanical Engineering and 2D Crystal Consortium (2DCC), Materials Research Institute (MRI), The Pennsylvania State University, University Park, Pennsylvania 16802, United States*

Benjamin Huet − *2D Crystal Consortium (2DCC), Materials Research Institute (MRI) and Applied Research Laboratory (ARL), The Pennsylvania State University, University Park, Pennsylvania 16802, United States;* orcid.org/0000-0003-4084-5705

Nadire Nayir − *Department of Mechanical Engineering and 2D Crystal Consortium (2DCC), Materials Research Institute (MRI), The Pennsylvania State University, University Park, Pennsylvania 16802, United States; Department of Physics, Karamanoglu Mehmetbey University, Karaman, Turkey 7000;* orcid.org/0000-0002-3621-2481

Swarit Dwivedi − *Department of Mechanical Engineering and 2D Crystal Consortium (2DCC), Materials Research Institute (MRI), The Pennsylvania State University, University Park, Pennsylvania 16802, United States;* orcid.org/0000-0002-4639-5576

Danielle Reifsnyder Hickey − *Department of Materials Science and Engineering, The Pennsylvania State University, University Park, Pennsylvania 16802, United States; 2D Crystal Consortium (2DCC), Materials Research Institute (MRI) and Department of Chemistry, The Pennsylvania State University, University Park, Pennsylvania 16802, United States;* orcid.org/0000-0002-8962-1473

Chenhao Qian − *Department of Materials Science and Engineering, The Pennsylvania State University, University Park, Pennsylvania 16802, United States*

David W. Snyder − *Applied Research Laboratory (ARL), The Pennsylvania State University, University Park, Pennsylvania 16802, United States*

Slava V. Rotkin − *Materials Research Institute and Department of Engineering Science & Mechanics, The Pennsylvania State University, University Park, Pennsylvania 16802, United States;* orcid.org/0000-0001-7221-1091

Joan M. Redwing − *Department of Materials Science and Engineering, The Pennsylvania State University, University Park, Pennsylvania 16802, United States; 2D Crystal Consortium (2DCC), Materials Research Institute (MRI), The Pennsylvania State University, University Park, Pennsylvania 16802, United States;* orcid.org/0000-0002-7906-452X

Adri C. T. van Duin − *Department of Materials Science and Engineering, The Pennsylvania State University, University Park, Pennsylvania 16802, United States; Department of Mechanical Engineering and 2D Crystal Consortium (2DCC), Materials Research Institute (MRI), The Pennsylvania State University, University Park, Pennsylvania 16802, United States;* orcid.org/0000-0002-3478-4945

Complete contact information is available at: https://pubs.acs.org/10.1021/acsnano.2c12621

Author Contributions

The manuscript was written through contributions of all authors. All authors have given approval to the final version of the manuscript.

Notes

The authors declare no competing financial interest.

ACKNOWLEDGMENTS

This work is carried out with the funding acquired from the National Science Foundation (NSF) through a CAREER DMR-1654107 grant. All the authors would also like to acknowledge the financial support from the NSF through Penn State 2D Crystal Consortium-Materials Innovation Platform (2DCC-MIP) under DMR-1539916 and DMR-2039351. Authors also acknowledge the Applied Research Laboratory (ARL), the Nanofabrication Laboratory, and the Materials Characterization Lab (MCL) facilities of Pennsylvania State University for the CVD graphene and characterization equipment. D.R.H. also acknowledges start-up funds from the Penn State Eberly College of Science, Department of Chemistry, and Materials Research Institute. The sSNOM work was partially supported by NSF MRSEC (DMR-2011839). S.V.R. acknowledges partial support from a College of Engineering Multidisciplinary Seed Grant by Penn State University.

REFERENCES

(1) Wang, Y.; Li, L.; Yao, W.; Song, S.; Sun, J. T.; Pan, J.; Ren, X.; Li, C.; Okunishi, E.; Wang, Y.-Q.; Wang, E.; Shao, Y.; Zhang, Y. Y.; Yang, H.; Schwier, E. F.; Iwasawa, H.; Shimada, K.; Taniguchi, M.; Cheng, Z.; Zhou, S.; Du, S.; Pennycook, S. J.; Pantelides, S. T.; Gao, H.-J. Monolayer PtSe2, a New Semiconducting Transition-Metal-Dichalcogenide, Epitaxially Grown by Direct Selenization of Pt. *Nano Lett.* **2015**, *15* (6), 4013−4018.

(2) Radisavljevic, B.; Radenovic, A.; Brivio, J.; Giacometti, V.; Kis, A. Single-Layer MoS2 Transistors. *Nat. Nanotechnol.* **2011**, *6* (3), 147−150.

(3) Sebastian, A.; Pendurthi, R.; Choudhury, T. H.; Redwing, J. M.; Das, S. Benchmarking Monolayer MoS2 and WS2 Field-Effect Transistors. *Nat. Commun.* **2021**, *12* (1), 693.

(4) Lv, R.; Robinson, J. A.; Schaak, R. E.; Sun, D.; Sun, Y.; Mallouk, T. E.; Terrones, M. Transition Metal Dichalcogenides and Beyond: Synthesis, Properties, and Applications of Single- and Few-Layer Nanosheets. *Acc. Chem. Res.* **2015**, *48* (1), 56−64.

(5) Lin, Z.; McCreary, A.; Briggs, N.; Subramanian, S.; Zhang, K.; Sun, Y.; Li, X.; Borys, N. J.; Yuan, H.; Fullerton-Shirey, S. K.; Chernikov, A.; Zhao, H.; McDonnell, S.; Lindenberg, A. M.; Xiao, K.; LeRoy, B. J.; Drndić, M.; Hwang, J. C. M.; Park, J.; Chhowalla, M.; Schaak, R. E.; Javey, A.; Hersam, M. C.; Robinson, J.; Terrones, M. 2D Materials Advances: From Large Scale Synthesis and Controlled Heterostructures to Improved Characterization Techniques, Defects and Applications. *2D Mater.* **2016**, *3* (4), 042001.

(6) Perkins, F. K.; Friedman, A. L.; Cobas, E.; Campbell, P. M.; Jernigan, G. G.; Jonker, B. T. Chemical Vapor Sensing with Monolayer MoS2. *Nano Lett.* **2013**, *13* (2), 668−673.

(7) Hanbicki, A. T.; Currie, M.; Kioseoglou, G.; Friedman, A. L.; Jonker, B. T. Measurement of High Exciton Binding Energy in the Monolayer Transition-Metal Dichalcogenides WS2 and WSe2. *Solid State Commun.* **2015**, *203*, 16−20.

(8) Li, Z.; Xiao, Y.; Gong, Y.; Wang, Z.; Kang, Y.; Zu, S.; Ajayan, P. M.; Nordlander, P.; Fang, Z. Active Light Control of the MoS2Monolayer Exciton Binding Energy. *ACS Nano* **2015**, *9* (10), 10158−10164.

(9) Kang, K.; Xie, S.; Huang, L.; Han, Y.; Huang, P. Y.; Mak, K. F.; Kim, C.-J.; Muller, D.; Park, J. High-Mobility Three-Atom-Thick

Semiconducting Films with Wafer-Scale Homogeneity. *Nature* **2015**, *520* (7549), 656−660.
(10) Dumcenco, D.; Ovchinnikov, D.; Marinov, K.; Lazić, P.; Gibertini, M.; Marzari, N.; Sanchez, O. L.; Kung, Y.-C.; Krasnozhon, D.; Chen, M.-W.; Bertolazzi, S.; Gillet, P.; Fontcuberta i Morral, A.; Radenovic, A.; Kis, A. Large-Area Epitaxial Monolayer MoS2. *ACS Nano* **2015**, *9* (4), 4611−4620.
(11) Choudhury Tanushree, H.; Huet, B.; Zhang, X.; Bansal, A.; Redwing, J. M. Scalable Synthesis of 2D Materials. In *2D Materials for Electronics, Sensors and Devices: Synthesis, Characterization, Fabrication and Application*; Elsevier, 2022; pp 1−52.
(12) Chubarov, M.; Choudhury, T. H.; Hickey, D. R.; Bachu, S.; Zhang, T.; Sebastian, A.; Bansal, A.; Zhu, H.; Trainor, N.; Das, S.; Terrones, M.; Alem, N.; Redwing, J. M. Wafer-Scale Epitaxial Growth of Unidirectional WS2Monolayers on Sapphire. *ACS Nano* **2021**, *15* (2), 2532−2541.
(13) Zhang, X.; Choudhury, T. H.; Chubarov, M.; Xiang, Y.; Jariwala, B.; Zhang, F.; Alem, N.; Wang, G.-C.; Robinson, J. A.; Redwing, J. M. Diffusion-Controlled Epitaxy of Large Area Coalesced WSe2Monolayers on Sapphire. *Nano Lett.* **2018**, *18* (2), 1049−1056.
(14) Shi, Y.; Zhou, W.; Lu, A.-Y.; Fang, W.; Lee, Y.-H.; Hsu, A. L.; Kim, S. M.; Kim, K. K.; Yang, H. Y.; Li, L.-J.; Idrobo, J.-C.; Kong, J. Van Der Waals Epitaxy of MoS2 Layers Using Graphene As Growth Templates. *Nano Lett.* **2012**, *12* (6), 2784−2791.
(15) Zhou, J.; Lin, J.; Huang, X.; Zhou, Y.; Chen, Y.; Xia, J.; Wang, H.; Xie, Y.; Yu, H.; Lei, J.; Wu, D.; Liu, F.; Fu, Q.; Zeng, Q.; Hsu, C.-H.; Yang, C.; Lu, L.; Yu, T.; Shen, Z.; Lin, H.; Yakobson, B. I.; Liu, Q.; Suenaga, K.; Liu, G.; Liu, Z. A Library of Atomically Thin Metal Chalcogenides. *Nature* **2018**, *556* (7701), 355−359.
(16) Zhang, X.; Zhang, F.; Wang, Y.; Schulman, D. S.; Zhang, T.; Bansal, A.; Alem, N.; Das, S.; Crespi, V. H.; Terrones, M.; Redwing, J. M. Defect-Controlled Nucleation and Orientation of WSe2 on HBN: A Route to Single-Crystal Epitaxial Monolayers. *ACS Nano* **2019**, *13* (3), 3341−3352.
(17) Bianco, G. V.; Losurdo, M.; Giangregorio, M. M.; Sacchetti, A.; Prete, P.; Lovergine, N.; Capezzuto, P.; Bruno, G. Direct Epitaxial CVD Synthesis of Tungsten Disulfide on Epitaxial and CVD Graphene. *RSC Adv.* **2015**, *5* (119), 98700−98708.
(18) Eichfeld, S. M.; Hossain, L.; Lin, Y.-C.; Piasecki, A. F.; Kupp, B.; Birdwell, A. G.; Burke, R. A.; Lu, N.; Peng, X.; Li, J.; Azcatl, A.; McDonnell, S.; Wallace, R. M.; Kim, M. J.; Mayer, T. S.; Redwing, J. M.; Robinson, J. A. Highly Scalable, Atomically Thin WSe2 Grown via Metal-Organic Chemical Vapor Deposition. *ACS Nano* **2015**, *9* (2), 2080−2087.
(19) Tan, J.; Li, S.; Liu, B.; Cheng, H.-M. Structure, Preparation, and Applications of 2D Material-Based Metal-Semiconductor Heterostructures. *Small Structures* **2021**, *2* (1), 2000093.
(20) Thanh, T. D.; Chuong, N. D.; Hien, H. V.; Kshetri, T.; Tuan, L. H.; Kim, N. H.; Lee, J. H. Recent Advances in Two-Dimensional Transition Metal Dichalcogenides-Graphene Heterostructured Materials for Electrochemical Applications. *Prog. Mater. Sci.* **2018**, *96*, 51−85.
(21) Sun, X.; Zhang, B.; Li, Y.; Luo, X.; Li, G.; Chen, Y.; Zhang, C.; He, J. Tunable Ultrafast Nonlinear Optical Properties of Graphene/MoS2 van Der Waals Heterostructures and Their Application in Solid-State Bulk Lasers. *ACS Nano* **2018**, *12* (11), 11376−11385.
(22) Shi, Z.; Huang, H.; Wang, C.; Huo, M.; Ho, S.-H.; Tsai, H.-S. Heterogeneous Transition Metal Dichalcogenides/Graphene Composites Applied to the Metal-Ion Batteries. *Chemical Engineering Journal* **2022**, *447*, 137469.
(23) Tang, H.-L.; Chiu, M.-H.; Tseng, C.-C.; Yang, S.-H.; Hou, K.-J.; Wei, S.-Y.; Huang, J.-K.; Lin, Y.-F.; Lien, C.-H.; Li, L.-J. Multilayer Graphene-WSe2 Heterostructures for WSe2 Transistors. *ACS Nano* **2017**, *11* (12), 12817−12823.
(24) Lin, Y.-C.; Chang, C.-Y. S.; Ghosh, R. K.; Li, J.; Zhu, H.; Addou, R.; Diaconescu, B.; Ohta, T.; Peng, X.; Lu, N.; Kim, M. J.; Robinson, J. T.; Wallace, R. M.; Mayer, T. S.; Datta, S.; Li, L.-J.; Robinson, J. A. Atomically Thin Heterostructures Based on Single-Layer Tungsten Diselenide and Graphene. *Nano Lett.* **2014**, *14* (12), 6936−6941.
(25) Yang, S.-H.; Yang, F.-S.; Tang, H.-L.; Chiu, M.-H.; Lee, K.-C.; Li, M.; Lin, C.-Y.; Li, L.-J.; Tung, V.; Xu, Y.; Shi, Y.; Lien, C.-H.; Lin, Y.-F. Performance Limits and Potential of Multilayer Graphene-Tungsten Diselenide Heterostructures. *Advanced Electronic Materials* **2021**, *7* (12), 2100355.
(26) Azizi, A.; Eichfeld, S.; Geschwind, G.; Zhang, K.; Jiang, B.; Mukherjee, D.; Hossain, L.; Piasecki, A. F.; Kabius, B.; Robinson, J. A.; Alem, N. Freestanding van Der Waals Heterostructures of Graphene and Transition Metal Dichalcogenides. *ACS Nano* **2015**, *9* (5), 4882−4890.
(27) Kim, S.-Y.; Kim, J. H.; Lee, S.; Kwak, J.; Jo, Y.; Yoon, E.; Lee, G.-D.; Lee, Z.; Kwon, S.-Y. The Impact of Substrate Surface Defects on the Properties of Two-Dimensional van Der Waals Heterostructures. *Nanoscale* **2018**, *10* (40), 19212−19219.
(28) Kim, J. H.; Kim, S.-Y.; Cho, Y.; Park, H. J.; Shin, H.-J.; Kwon, S.-Y.; Lee, Z. Interface-Driven Partial Dislocation Formation in 2D Heterostructures. *Adv. Mater.* **2019**, *31* (15), 1807486.
(29) Zhang, Y.; Zhang, X.; Deng, C.; Ge, Q.; Huang, J.; Lu, J.; Lin, G.; Weng, Z.; Zhang, X.; Cai, W. Effect of Graphene Grain Boundaries on MoS2graphene Heterostructures. *Chinese Phys. B* **2020**, *29* (6), 067403.
(30) Huet, B.; Raskin, J.-P. Role of Cu Foil In-Situ Annealing in Controlling the Size and Thickness of CVD Graphene Domains. *Carbon* **2018**, *129*, 270−280.
(31) Ta, H. Q.; Perello, D. J.; Duong, D. L.; Han, G. H.; Gorantla, S.; Nguyen, V. L.; Bachmatiuk, A.; Rotkin, S. V.; Lee, Y. H.; Rümmeli, M. H. Stranski-Krastanov and Volmer-Weber CVD Growth Regimes To Control the Stacking Order in Bilayer Graphene. *Nano Lett.* **2016**, *16* (10), 6403−6410.
(32) Liu, J.; Wang, Z.; Ling, D.; Wei, D.; Lv, W.; Kang, X.; Qi, F.; Ding, S.; Hao, X.; Li, P.; Chen, Y. Synchronous Growth of 30°-Twisted Bilayer Graphene Domains with Millimeter Scale. *2D Mater.* **2021**, *8* (2), 021002.
(33) Annevelink, E.; Johnson, H. T.; Ertekin, E. Topologically Derived Dislocation Theory for Twist and Stretch Moir\'e Superlattices in Bilayer Graphene. *Phys. Rev. B* **2020**, *102* (18), 184107.
(34) Weckbecker, D.; Gupta, R.; Rost, F.; Sharma, S.; Shallcross, S. Dislocation and Node States in Bilayer Graphene Systems. *Phys. Rev. B* **2019**, *99* (19), 195405.
(35) Yoo, H.; Engelke, R.; Carr, S.; Fang, S.; Zhang, K.; Cazeaux, P.; Sung, S. H.; Hovden, R.; Tsen, A. W.; Taniguchi, T.; Watanabe, K.; Yi, G.-C.; Kim, M.; Luskin, M.; Tadmor, E. B.; Kaxiras, E.; Kim, P. Atomic and Electronic Reconstruction at the van Der Waals Interface in Twisted Bilayer Graphene. *Nat. Mater.* **2019**, *18* (5), 448−453.
(36) Liu, J.; Zhang, X.; Zhang, Y.; Ren, Q.; Jin, Y.; Zhao, P. Inherent Strains in Chemical-Vapor-Deposited Bilayer Graphene on Cu. *Carbon* **2021**, *184*, 109−114.
(37) Huet, B.; Bachu, S.; Alem, N.; Snyder, D. W.; Redwing, J. M. MOCVD of WSe2 Crystals on Highly Crystalline Single- and Multi-Layer CVD Graphene. *Carbon* **2023**, *202*, 150−160.
(38) van Duin, A. C. T.; Dasgupta, S.; Lorant, F.; Goddard, W. A. ReaxFF: A Reactive Force Field for Hydrocarbons. *J. Phys. Chem. A* **2001**, *105* (41), 9396−9409.
(39) Sun, H.-B.; Wu, J.; Han, Y.; Wang, J.-Y.; Song, F.-Q.; Wan, J.-G. Nonisothermal Synthesis of AB-Stacked Bilayer Graphene on Cu Foils by Atmospheric Pressure Chemical Vapor Deposition. *J. Phys. Chem. C* **2014**, *118* (26), 14655−14661.
(40) Huang, W.; Liu, Z.-F.; Yang, Z.-Y. Top or underneath? Revealing the Structure of Multilayer Graphene Domains with Atomic Force Microscopy and Theoretical Analysis. *Carbon* **2016**, *99*, 131−137.
(41) Li, J.; Zhuang, J.; Shen, C.; Tian, Y.; Que, Y.; Ma, R.; Pan, J.; Zhang, Y.; Wang, Y.; Du, S.; Ding, F.; Gao, H.-J. Impurity-Induced Formation of Bilayered Graphene on Copper by Chemical Vapor Deposition. *Nano Res.* **2016**, *9* (9), 2803−2810.
(42) Dai, X.; Mitchell, I.; Kim, S.; An, H.; Ding, F. Multilayer Graphene Sunk Growth on Cu(111) Surface. *Carbon* **2022**, *199*, 233.

https://doi.org/10.1021/acsnano.2c12621
ACS Nano 2023, 17, 12140−12150

(43) Zhang, F.; Wang, Y.; Erb, C.; Wang, K.; Moradifar, P.; Crespi, V. H.; Alem, N. Full Orientation Control of Epitaxial MoS2 on HBN Assisted by Substrate Defects. *Phys. Rev. B* **2019**, *99* (15), 155430.
(44) Gao, Z.; Zhao, M.-Q.; Ashik, M. M. A.; Johnson, A. T. C. Recent Advances in the Properties and Synthesis of Bilayer Graphene and Transition Metal Dichalcogenides. *J. Phys. Mater.* **2020**, *3* (4), 042003.
(45) Butz, B.; Dolle, C.; Niekiel, F.; Weber, K.; Waldmann, D.; Weber, H. B.; Meyer, B.; Spiecker, E. Dislocations in Bilayer Graphene. *Nature* **2014**, *505* (7484), 533−537.
(46) Brown, L.; Hovden, R.; Huang, P.; Wojcik, M.; Muller, D. A.; Park, J. Twinning and Twisting of Tri- and Bilayer Graphene. *Nano Lett.* **2012**, *12* (3), 1609−1615.
(47) Alden, J. S.; Tsen, A. W.; Huang, P. Y.; Hovden, R.; Brown, L.; Park, J.; Muller, D. A.; McEuen, P. L. Strain Solitons and Topological Defects in Bilayer Graphene. *Proc. Natl. Acad. Sci. U.S.A.* **2013**, *110* (28), 11256−11260.
(48) Lin, J.; Fang, W.; Zhou, W.; Lupini, A. R.; Idrobo, J. C.; Kong, J.; Pennycook, S. J.; Pantelides, S. T. AC/AB Stacking Boundaries in Bilayer Graphene. *Nano Lett.* **2013**, *13* (7), 3262−3268.
(49) Kushima, A.; Qian, X.; Zhao, P.; Zhang, S.; Li, J. Ripplocations in van Der Waals Layers. *Nano Lett.* **2015**, *15* (2), 1302−1308.
(50) McHugh, J. G.; Mouratidis, P.; Jolley, K. Ripplocations in Layered Materials: Sublinear Scaling and Basal Climb. *Phys. Rev. B* **2021**, *103* (19), 195436.
(51) Ostadhossein, A.; Rahnamoun, A.; Wang, Y.; Zhao, P.; Zhang, S.; Crespi, V. H.; van Duin, A. C. T. ReaxFF Reactive Force-Field Study of Molybdenum Disulfide (MoS2). *J. Phys. Chem. Lett.* **2017**, *8* (3), 631−640.
(52) Kumar, H.; Dong, L.; Shenoy, V. B. Limits of Coherency and Strain Transfer in Flexible 2D van Der Waals Heterostructures: Formation of Strain Solitons and Interlayer Debonding. *Sci. Rep* **2016**, *6* (1), 21516.
(53) Yang, L.; Xu, H.; Liu, K.; Gao, D.; Huang, Y.; Zhou, Q.; Wu, Z. Molecular Dynamics Simulation on the Formation and Development of Interlayer Dislocations in Bilayer Graphene. *Nanotechnology* **2020**, *31* (12), 125704.
(54) Feng, S.; Xu, Z. Pattern Development and Control of Strained Solitons in Graphene Bilayers. *Nano Lett.* **2021**, *21* (4), 1772−1777.
(55) Dai, S.; Xiang, Y.; Srolovitz, D. J. Structure and Energetics of Interlayer Dislocations in Bilayer Graphene. *Phys. Rev. B* **2016**, *93* (8), 085410.
(56) Lebedeva, I. V.; Popov, A. M. Commensurate-Incommensurate Phase Transition and a Network of Domain Walls in Bilayer Graphene with a Biaxially Stretched Layer. *Phys. Rev. B* **2019**, *99* (19), 195448.
(57) Lebedeva, I. V.; Lebedev, A. V.; Popov, A. M.; Knizhnik, A. A. Dislocations in Stacking and Commensurate-Incommensurate Phase Transition in Bilayer Graphene and Hexagonal Boron Nitride. *Phys. Rev. B* **2016**, *93* (23), 235414.
(58) Meyer, J. C.; Geim, A. K.; Katsnelson, M. I.; Novoselov, K. S.; Obergfell, D.; Roth, S.; Girit, C.; Zettl, A. On the Roughness of Single- and Bi-Layer Graphene Membranes. *Solid State Commun.* **2007**, *143* (1), 101−109.
(59) Huet, B.; Raskin, J.-P. Role of the Cu Substrate in the Growth of Ultra-Flat Crack-Free Highly-Crystalline Single-Layer Graphene. *Nanoscale* **2018**, *10* (46), 21898−21909.
(60) Yuk, J. M.; Jeong, H. Y.; Kim, N. Y.; Park, H. J.; Kim, G.; Shin, H. S.; Ruoff, R. S.; Lee, J. Y.; Lee, Z. Superstructural Defects and Superlattice Domains in Stacked Graphene. *Carbon* **2014**, *80*, 755−761.
(61) Warner, J. H.; Margine, E. R.; Mukai, M.; Robertson, A. W.; Giustino, F.; Kirkland, A. I. Dislocation-Driven Deformations in Graphene. *Science* **2012**, *337* (6091), 209−212.
(62) Lehtinen, O.; Kurasch, S.; Krasheninnikov, A. V.; Kaiser, U. Atomic Scale Study of the Life Cycle of a Dislocation in Graphene from Birth to Annihilation. *Nat. Commun.* **2013**, *4* (1), 2098.
(63) Robertson, A. W.; Lee, G.-D.; He, K.; Fan, Y.; Allen, C. S.; Lee, S.; Kim, H.; Yoon, E.; Zheng, H.; Kirkland, A. I.; Warner, J. H. Partial Dislocations in Graphene and Their Atomic Level Migration Dynamics. *Nano Lett.* **2015**, *15* (9), 5950−5955.
(64) Na, M. Y.; Lee, S.-M.; Kim, D. H.; Chang, H. J. Dark-Field Transmission Electron Microscopy Imaging Technique to Visualize the Local Structure of Two-Dimensional Material; Graphene. *Applied Microscopy* **2015**, *45* (1), 23−31.
(65) Shevitski, B.; Mecklenburg, M.; Hubbard, W. A.; White, E. R.; Dawson, B.; Lodge, M. S.; Ishigami, M.; Regan, B. C. Dark-Field Transmission Electron Microscopy and the Debye-Waller Factor of Graphene. *Phys. Rev. B* **2013**, *87* (4), 045417.
(66) Sung, S. H.; Schnitzer, N.; Brown, L.; Park, J.; Hovden, R. Stacking, Strain, and Twist in 2D Materials Quantified by 3D Electron Diffraction. *Phys. Rev. Materials* **2019**, *3* (6), 064003.
(67) Schweizer, P.; Dolle, C.; Spiecker, E. In Situ Manipulation and Switching of Dislocations in Bilayer Graphene. *Science Advances* **2018**, *4* (8), eaat4712.
(68) Lee, S.-M.; Kim, S.-M.; Na, M. Y.; Chang, H. J.; Kim, K.-S.; Yu, H.; Lee, H.-J.; Kim, J.-H. Materialization of Strained CVD-Graphene Using Thermal Mismatch. *Nano Res.* **2015**, *8* (6), 2082−2091.
(69) Huet, B.; Raskin, J.-P.; Snyder, D. W.; Redwing, J. M. Fundamental Limitations in Transferred CVD Graphene Caused by Cu Catalyst Surface Morphology. *Carbon* **2020**, *163*, 95−104.
(70) Ryu, G. H.; Park, H. J.; Kim, N. Y.; Lee, Z. Atomic Resolution Imaging of Rotated Bilayer Graphene Sheets Using a Low KV Aberration-Corrected Transmission Electron Microscope. *Applied Microscopy* **2012**, *42* (4), 218−222.
(71) Chenoweth, K.; van Duin, A. C. T.; Goddard, W. A. ReaxFF Reactive Force Field for Molecular Dynamics Simulations of Hydrocarbon Oxidation. *J. Phys. Chem. A* **2008**, *112* (5), 1040−1053.
(72) Senftle, T. P.; Hong, S.; Islam, M. M.; Kylasa, S. B.; Zheng, Y.; Shin, Y. K.; Junkermeier, C.; Engel-Herbert, R.; Janik, M. J.; Aktulga, H. M.; Verstraelen, T.; Grama, A.; van Duin, A. C. T. The ReaxFF Reactive Force-Field: Development, Applications and Future Directions. *npj Comput. Mater.* **2016**, *2* (1), 1−14.
(73) Xu, H.; Al-Ghalith, J.; Dumitrică, T. Smooth Sliding and Superlubricity in the Nanofriction of Collapsed Carbon Nanotubes. *Carbon* **2018**, *134*, 531−535.
(74) Humphrey, W.; Dalke, A.; Schulten, K. VMD: Visual Molecular Dynamics. *J. Mol. Graphics* **1996**, *14* (1), 33−38.
(75) Stukowski, A. Visualization and Analysis of Atomistic Simulation Data with OVITO-the Open Visualization Tool. *Modelling Simul. Mater. Sci. Eng.* **2010**, *18* (1), 015012.
(76) te Velde, G.; Bickelhaupt, F. M.; Baerends, E. J.; Fonseca Guerra, C.; van Gisbergen, S. J. A.; Snijders, J. G.; Ziegler, T. Chemistry with ADF. *J. Comput. Chem.* **2001**, *22* (9), 931−967.
(77) Thompson, A. P.; Plimpton, S. J.; Mattson, W. General Formulation of Pressure and Stress Tensor for Arbitrary Many-Body Interaction Potentials under Periodic Boundary Conditions. *J. Chem. Phys.* **2009**, *131* (15), 154107.
(78) *ADF: accurate & efficient DFT, with great GUI & expert support*; Software for Chemistry & Materials; https://www.scm.com/product/adf/ (accessed 2022−12−07).

https://doi.org/10.1021/acsnano.2c12621
ACS Nano 2023, 17, 12140−12150